

# Pyrite as promising monograin layer solar cell absorber material for *in-situ* solar cell fabrication on the Moon

Katriin Kristmann<sup>a,\*</sup>, Taavi Raadik<sup>a</sup>, Mare Altosaar<sup>a</sup>, Maarja Grossberg-Kuusik<sup>a</sup>, Jüri Krustok<sup>a,b</sup>, Maris Pilvet<sup>a</sup>, Valdek Mikli<sup>a</sup>, Marit Kauk-Kuusik<sup>a</sup>, Adventit Makaya<sup>c</sup>

<sup>a</sup> Department of Materials and Environmental Technology, Tallinn University of Technology, Ehitajate Tee 5, 19086, Tallinn, Estonia

<sup>b</sup> Division of Physics, Tallinn University of Technology, Ehitajate Tee 5, 19086 Tallinn, Estonia

<sup>c</sup> European Space Research and Technology Centre (ESTEC), Keplerlaan 1, 2201 AZ, Noordwijk, the Netherlands

## ARTICLE INFO

### Keywords:

Monograin layer solar cell  
Molten salt synthesis  
FeS<sub>2</sub>  
In-situ resource utilization  
Lunar base

## ABSTRACT

Reliable energy sources are needed in order to keep a Lunar Base on the run, and solar energy is one of the most attractive options. There are two ways to achieve it – to bring necessary solar panels from the Earth or find a way to produce them *in-situ* on the Moon from local resources. We propose the monograin layer (MGL) solar cell technology, that could be used for the *in-situ* production of solar panels on the Moon. One of the most promising compounds, that can be used as an absorber material in a monograin layer solar cell is pyrite FeS<sub>2</sub>. There are considerable amounts of iron and sulphur in the lunar regolith. Conditions for the synthesis-growth of FeS<sub>2</sub> monograin powders were found and are presented in this study. The synthesis-growth of FeS<sub>2</sub> powder at 740 °C in potassium iodide for one week followed by slow cooling to 575 °C and rapid cooling to the room temperature, resulted in single phase pyrite monograin powder. Powder crystals had round shape and the median size of about 50 μm was appropriate for making monograin layers. The produced FeS<sub>2</sub> MGLs were used as absorber layers in MGL solar cells with structure as graphite/FeS<sub>2</sub>/NiO/TCO and in FeS<sub>2</sub>/Pt Schottky diodes. Charge carrier concentration of  $6.2 \times 10^{16} \text{ cm}^{-3}$  was determined from capacitance-voltage measurements of FeS<sub>2</sub>/NiO heterostructure and  $2.5 \times 10^{17} \text{ cm}^{-3}$  from FeS<sub>2</sub>/Pt Schottky diode.

## 1. Introduction

Securing a permanent lunar outpost is among the goals for future interplanetary space flights and the exploration of Mars and further celestial objects [1,2]. Therein, establishing reliable energy supply on the Moon will define the feasibility of the mission. It is extremely practical to manage with resources that are available in the lunar soil (or regolith) to lower the price of the lunar village mission.

It is especially important to establish a reliable energy supply. Continuous photovoltaic solar energy production is possible on the Moon because some areas around the lunar south pole are constantly illuminated by the Sun [3]. Producing solar cell materials and panels *in situ* from elements of lunar regolith would be the best way to use the available resources, as the cost of sending them from Earth is extremely high [4]. This study was aimed to the *in-situ* resource utilization (ISRU) approach to produce solar energy on the Moon. One promising possibility is to use the monograin layer (MGL) solar cell technology [5–7]. MGL solar cell has a superstrate solar cell structure: *back*

*contact/absorber/buffer/transparent conductive oxide*. The structure is glued on a supportive substrate (glass or polymer film). The MGL solar cell absorber is a monolayer of nearly unisize semiconductor powder crystals fixed in a thinner-than-crystal-size layer of epoxy (or some other polymer) (Fig. 1.) [8]. The powder crystals' surfaces are coated with a thin layer of a buffer material (ordinarily via solution deposition under continuous stirring) for creating the semiconductor *p/n* junction. After the buffer layer deposition (followed by soft heat-treatment) each covered crystal is a tiny photovoltaic cell. Therefore, the MGL technology has an advantage compared to other thin film solar cell technologies - it allows to separate (geographically) processes of absorber (powder) production from solar cell module formation. The MGL solar cell structure enables to manufacture flexible, lightweight, and cost-efficient solar panels. The technology combines advantages of high-efficiency single-crystalline material and of low-cost roll-to-roll panel production. Thus, it enables to cover vast areas with minimum cost [8]. All the MGL solar cell production processes are well performable in the low pressure or vacuum environment. When the synthesis ampoules have been degassed under dynamic vacuum and sealed, then they are inserted

\* Corresponding author.

E-mail address: [katriin.kristmann@taltech.ee](mailto:katriin.kristmann@taltech.ee) (K. Kristmann).

<https://doi.org/10.1016/j.actaastro.2022.07.043>

Received 11 March 2022; Received in revised form 15 July 2022; Accepted 25 July 2022

Available online 6 August 2022

0094-5765/© 2022 IAA. Published by Elsevier Ltd. All rights reserved.

**Acronyms/Abbreviations**

EDX	Energy-dispersive X-ray spectroscopy
HR-SEM	High resolution scanning electron microscope
ISRU	<i>In-Situ</i> Resources Utilization
MGL	monograin layer
TCO	transparent conductive oxide
KI	potassium iodide
XRD	X-ray diffraction
NiO	nickel oxide
PCE	power conversion efficiency

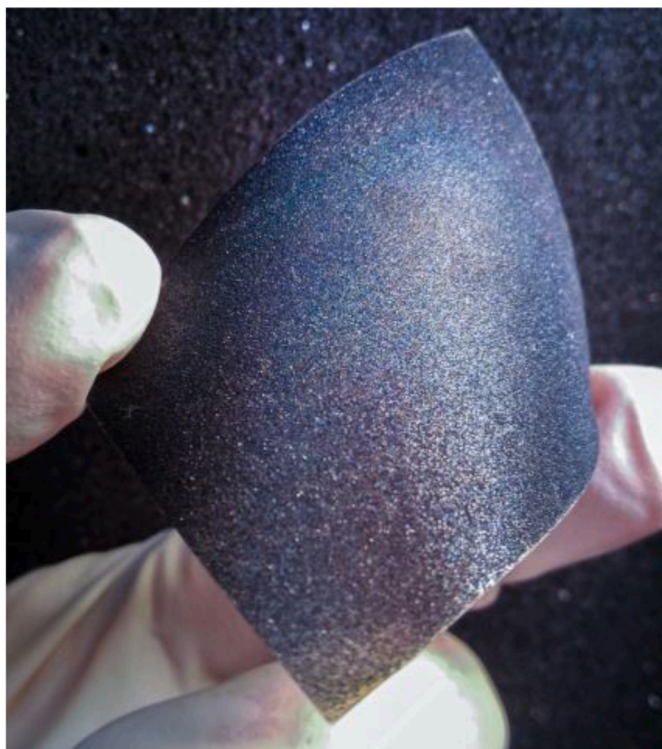


Fig. 1. Semi-finished MGL solar cell without encapsulant.

in a high-temperature furnace, where the gravity conditions are not considered to play an important role. Operating the furnace in vacuum will minimize the heat loss. Precise studies about the effects of low pressure and low gravity on the fabrication of MGL solar cells are in progress in the near future in coordination with the European Space Agency. First tests about the suitability of MGL solar cells for space applications was evaluated by T. Raadik et al. [9], where the tests were made in conditions simulating the lunar environment. Based on the results of this work [9] the European Space Agency showed remarkable interest in the monograin solar cell technology due to its advantages.

One promising candidate for the MGL solar cell absorber material is pyrite ( $\text{FeS}_2$ ). Lunar soil has a high content of iron (Fe) at the lunar mare and sulphur (S) at highland areas [10]. Furthermore, most of the elements that are present on Earth can also be found from the Moon's soil [11,12]. Therefore, it is possible to harvest most of the necessary elements for solar cell production *in situ* from the lunar soil, starting from absorber material and completing with an antireflective surface coating.

Pyrite is a semiconductor material that has all necessary parameters to be used in an efficient solar cell device. It has a suitable bandgap of 0.85–0.95 eV, high minority carrier diffusion length, high electron

mobility, and an even higher absorption coefficient than silicon – all making pyrite attractive as an absorber material to achieve potentially up to 25% energy conversion efficiency [13–16]. Despite high interest among material scientists and research efforts over three decades,  $\text{FeS}_2$  solar cells have never exceeded a PCE greater than 3% [17]. This poor conversion efficiency is mainly the result of poor photovoltage, which has not exceeded 0.3 V. Secondary phases, surface conduction phenomena, and undesired doping have been reported [17–19] as probable key issues behind the poor conversion efficiency. What's more, pyrite crystals and films have been reported to exhibit different conductivity types depending on the deposition and treatment regimes. Pyrite thin films usually have *p*-type conductivity while single crystals are commonly *n*-type [20]. The origin of the unintentional *p*-type doping of pyrite  $\text{FeS}_2$  is attributed to sulphur vacancies and formation of a fractured surface layer on an *n*-type pyrite single crystal. One of the main reasons for the creation of the inverse surface layer is iron's nearly equally stable oxidation states  $\text{Fe}^{2+}$  and  $\text{Fe}^{3+}$ , that makes the material's photo-electric properties difficult to control. When the  $\text{Fe}^{2+}$  ion oxidizes into  $\text{Fe}^{3+}$ , it lowers iron's coordination number with sulphur and creates energy levels close to the valence band edge, initiating the *p*-type conductivity [20–22]. In order to avoid the formation of  $\text{Fe}^{3+}$  and reduction of the Fe–S coordination, pyrite will be prepared in sulphur rich environment, proceeding with surface treatments that mitigate iron oxidation.

For  $\text{FeS}_2$  synthesis, it is necessary to extract iron and sulphur from regolith. According to literature, iron exists in the lunar soil in large quantities in the form of silicate and oxide phases. Troilite ( $\text{FeS}$ ) can also be found and is a highly suitable precursor for the synthesis of pyrite. So, it is required to add sulphur to  $\text{FeS}$  to form pyrite  $\text{FeS}_2$ . Sulphide minerals that are reported to be present in the lunar rocks include troilite, mackinawite, chalcopyrrhotite, sphalerite, chalcopyrite, and cubanite [23]. Sulphide minerals on the Moon can be found in the co-occurrence of magmatic Fe–Ti-oxides, as is in the case with Earth based samples, when they are compared with lunar mare basalts [24]. That way it is possible to use for example Clementine mission based Titanium maps [25] or infrared spectroscopy for in-orbit detection, as is being developed in the Polish Academy of Sciences [26]. It has been reported that sulphur can be extracted from regolith by heating it at 750–1100 °C [27, 28].

Purifying the lunar water for human and chemical consumption produces sulphur as a by-product.  $\text{H}_2\text{S}$  and  $\text{SO}_2$  are some of the primary pollutants of lunar water ice [29], which can be found in the bottom of the permanently shadowed craters near the lunar poles. Sulphide and sulphate pollutants constitute up to 20 wt% of the ice resource [29], and their removal by chemical processes produces sulphide gas, which can be reduced to elemental sulphur.

Another way of co-producing of sulphur is during the oxygen extraction from ilmenite-rich mare soils [30].

The MGL solar cell technology employs only a 50  $\mu\text{m}$  thick layer of  $\text{FeS}_2$ , so it can be calculated that a 10  $\text{m}^2$  large solar panel, that covers the dome of a living quarter and produces 700 W of power with 5% efficiency, will require 320 g of pyrite, or 235 g  $\text{FeS}$  and 85 g of S.

## 2. Materials and methods

### 2.1. Synthesis of $\text{FeS}_2$ microcrystals

In this study  $\text{FeS}_2$  monograin powders were synthesized from high-purity (5 N)  $\text{FeS}$  and S acquired from Alfa Aesar. The synthesis-growth process was performed in potassium iodide (KI) flux. The amounts of KI and the precursors for  $\text{FeS}_2$  formation were weighted considering that the volume of liquid phase  $V_{\text{liquid}}$  at the process temperature would be at least 0.6 of the volume of solid phase  $V_{\text{solid}}$ . This volume ratio of liquid and solid phases provides the condition, where repelling forces rise and exceed the capillary contracting forces between solid particles. In this case, the formation and growth of individual separate crystals is possible

[31]. Precursors FeS and S were weighted considering the formation of stoichiometric FeS<sub>2</sub>, mixed with KI, and loaded into a quartz ampoule. After degassing and heating up to approximately 80 °C, the ampoule was sealed and heated in a furnace up to 740 °C. It was kept at this temperature for one week. Then the furnace with ampoule was slowly cooled to 575 °C to ensure the pure FeS<sub>2</sub> pyrite phase in accordance with the published iron-sulphur phase diagrams [32,33]. This step is important, because iron and sulphur, in addition to pyrite, have an abundance of different compositions above sulphur melting temperature [34]. The furnace was kept at 575 °C for 24 h. After that the ampoule was cooled rapidly by quenching in water. As KI is water-soluble, leaching with DI water under ultrasonic agitation was used to release FeS<sub>2</sub> crystals from solid KI flux. Powders were rinsed multiple times until washing water remained clear and transparent. Reliability of the synthesis-growth process was confirmed by repeating it several times. The produced FeS<sub>2</sub> powder samples were very similar to each other and had a uniformly high quality.

## 2.2. Deposition and properties of NiO buffer layer

As synthesized pyrite FeS<sub>2</sub> microcrystals exhibited *n*-type conductivity detected by hot probe method, a *p*-type partner was needed for *p/n* junction formation. NiO was chosen as an option for the buffer layer, as it is a common *p*-type semiconductor material with a wide bandgap in the range of 3.6–4.0 eV [35] and utilizes abundant nontoxic elements that are readily available in the lunar soil [10]. NiO buffer layer was deposited by the successive ionic layer adsorption and reaction (SILAR) method from NiSO<sub>4</sub> solution at room temperature (RT). NiO deposition was based on the recipe proposed by Akaltun et al. [35] that utilized a 0.1 M Ni<sup>2+</sup> solution and hot water (85 °C) for NiO formation. Ni<sup>2+</sup> ions in this solution were in complex with NH<sub>4</sub><sup>+</sup> ions, while the ratio of [Ni<sup>2+</sup>] to [NH<sub>4</sub><sup>+</sup>] was equal to 1:10. The NiO deposition from 0.1 M Ni<sup>2+</sup> solution was fast and the deposited layers had cracks. Therefore, the NiSO<sub>4</sub> solution was diluted to 0.02 M to achieve thinner films with better coherence. [Ni<sup>2+</sup>]: [NH<sub>4</sub><sup>+</sup>] equal to 1:10 was kept constant and different deposition cycles of SILAR (20, 40 and 60 cycles) were applied for depositing films of different thickness, having continuous coverage and high transmittance.

## 2.3. Production of FeS<sub>2</sub> Schottky diodes and solar cells

Schottky diodes were prepared to measure the current-voltage characteristics and determine the pyrite crystals' work function and Fermi level. Various experimental measurements on pyrite's work function have reported different values between 3.9 eV [36] and 4.8–5.4 eV [37–39]. The work function of platinum is reported in the range of 5.6 eV–6.1 eV [40] and thus considered as a suitable metal junction partner for pyrite.

The FeS<sub>2</sub> monograin membranes for Schottky diodes and FeS<sub>2</sub>/NiO hetero-structures were made from sieved FeS<sub>2</sub>. The size fraction of 45–56 μm was used. Powder crystals were halfway embedded into a thin layer of epoxy leaving upper half of the crystals nondetached with epoxy and then covered with a junction partner material – metal or semiconductor. Pt layer was deposited by sputtering, NiO was deposited by the SILAR method.

## 2.4. Characterization of FeS<sub>2</sub> microcrystals and NiO films

The phase composition of the synthesized FeS<sub>2</sub> powders was studied by X-ray diffraction (XRD) and by Raman spectroscopy. For Raman studies, the Horiba's LabRam HR800 spectrometer equipped with a multichannel CCD detection system in the backscattering configuration was used. 532 nm laser line with spot size of 5 mm was applied for excitation. XRD patterns were recorded on a Rigaku Ultima IV diffractometer with Cu K<sub>α</sub> radiation ( $\lambda = 1.5406 \text{ \AA}$ ) operated at 40 kV and 40 mA in the  $2\theta$  range from 20 to 70° with a step of 0.002° and scanning

rate of 5° per minute. PDXL 2 software was used for the derivation of crystal structure information from the recorded XRD data. The chemical composition of powders was determined by energy dispersive X-ray spectroscopy (EDX) using Bruker Esprit 1.8 system. EDX analysis was performed over the crystals' surface to investigate the elemental distribution and compositional uniformity of different microcrystals. Several crystals' surfaces and bulk compositions were measured by a highly focused probe, EDX mapping was performed over large area of several crystals, mapping concluded the same results as from the single grain measurements. The morphology of crystals was studied with the high-resolution scanning electron microscope (HR-SEM) Zeiss ULTRA 55 with an accelerating voltage of 20 kV using a Röntec EDX XFlash 3001 detector.

Conductivity type of the material was determined by the hot probe method, where a sample crystal is placed between two indium probes. One probe is heated while the other stays at room temperature. The thermally excited free charge carriers will move by diffusion from the hot probe to the cold probe. These majority carriers define the electrical potential sign in the multimeter. The hot probe measurements were carried out for only a single grain at a time and not for the MGL membrane, to measure the conductivity of the FeS<sub>2</sub> single microcrystal. We tested multiple grains and the result was similar for all measurements.

## 2.5. Characterization of Schottky diodes and solar cells

To evaluate the main electrical characteristics of our devices, the current-voltage characteristics were measured under dark conditions and under illumination AM 1.5 G (100 mW/cm<sup>2</sup>) using a Newport Class AAA solar simulator system. I–V characteristics were recorded by a Keithley 2400 source meter.

Charge carrier density of the pyrite in devices was determined from capacitance-voltage measurements using Wayne Kerr 6500B potentiostat at different frequencies between 0.01 MHz and 10 MHz.

## 3. Results and discussion

### 3.1. Synthesis-growth of FeS<sub>2</sub> crystals in KI flux

The FeS<sub>2</sub> powder was synthesized from FeS and S (see the previous chapter) in KI as flux at 740 °C for one week. Formed crystals had a uniform round shape and smooth surfaces (see Fig. 2) – the morphology is suitable for monograin layer production. Roughly half of the gained powder material was in the desired size fraction of around 50 μm.

### 3.2. Raman, EDX and XRD results

Raman spectra of microcrystals synthesized in KI at 740 °C can be seen in Fig. 3. Raman peaks at 343, 379 and weak peaks at 350 and 430 cm<sup>-1</sup> are characteristic to the pyrite phase as reported in the literature [41,42]. Based on Raman analysis (Fig. 3) it can be concluded that the synthesis-growth of FeS<sub>2</sub> powder at 740 °C in KI followed by slow cooling to 575 °C resulted in pure FeS<sub>2</sub> pyrite phase. The formation of the secondary unwanted iron sulphide phases can be avoided if to proceed at high temperatures, provide the conditions for phase transition,

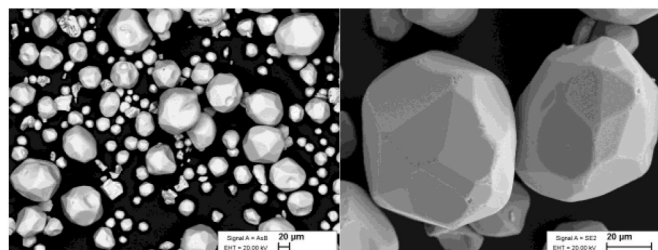


Fig. 2. SEM images of FeS<sub>2</sub> crystals synthesized in KI flux at 740 °C.

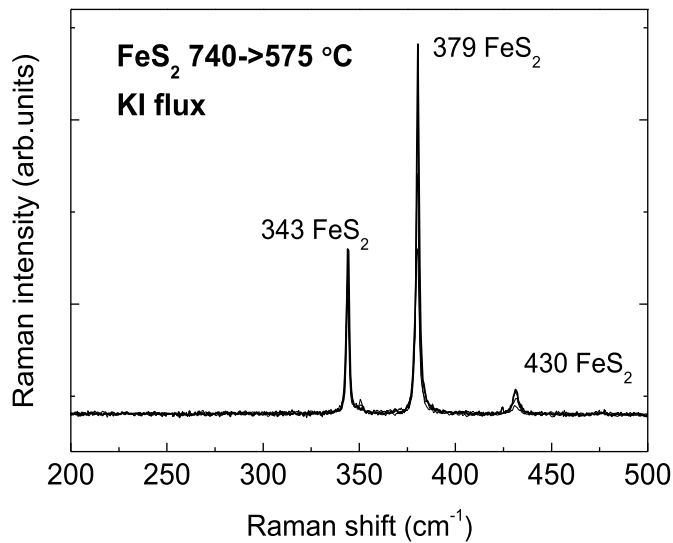


Fig. 3. Raman spectra of FeS<sub>2</sub> crystals synthesized at 740 °C in KI flux.

quench the material quickly and use a flux material that can be removed by leaching and rinsing with water.

According to the EDX results crystals synthesized at 740 °C had average composition of 33.71 at. % iron and 66.29 at. % sulphur.

The crystal structure of the microcrystals synthesized at 740 °C were analysed by XRD. The XRD pattern is presented in Fig. 4. The recorded lattice parameters  $a = b = c = 5.4154 \text{ \AA}$  confirm the cubic structure and are in good accordance with values reported in the literature [43–45]. Additionally, XRD and Raman results are in good correlation that there are no secondary phases in the synthesized crystals.

### 3.3. Electrical properties of the pyrite devices

Pyrite based Schottky diodes with Pt as junction partner were studied to assess the creation of a rectifying junction.

$I$ – $V$  curve of the structure of FeS<sub>2</sub>/Pt is presented in Fig. 5 (blue line). It can be seen from the shape of  $I$ – $V$  curve that a small rectifying junction is formed. However, the determination of the built-in voltage ( $V_{bi}$ ) from these measurements was not possible. The performance of the pyrite-

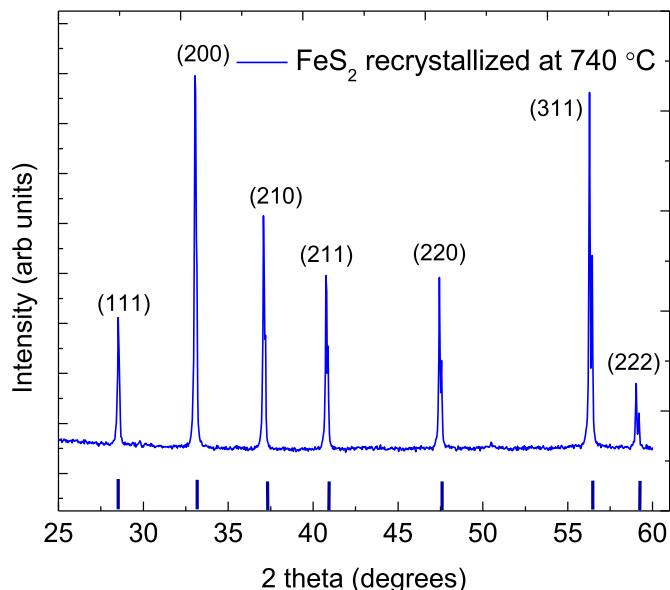


Fig. 4. XRD pattern of FeS<sub>2</sub> powders synthesized at 740 °C in KI flux.

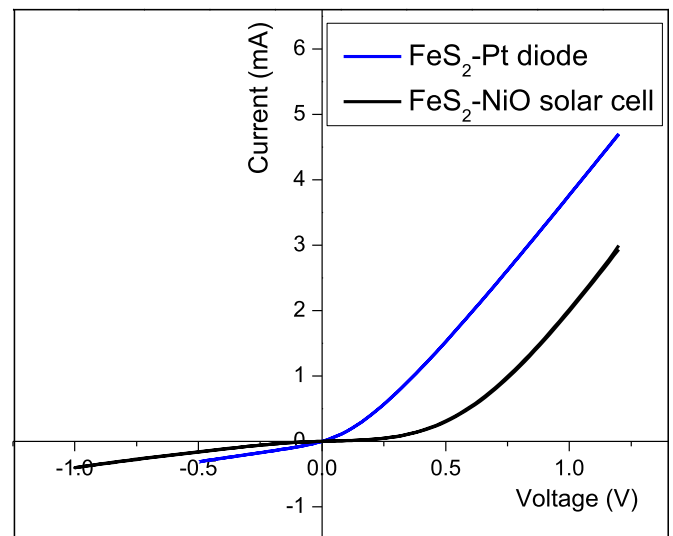


Fig. 5.  $I$ – $V$  curves of pyrite Schottky diode with Pt as junction partner (blue) and FeS<sub>2</sub>/NiO heterojunction solar cell (black). (For interpretation of the references to colour in this figure legend, the reader is referred to the Web version of this article.)

based diodes might have been limited due to Fermi level pinning, which has been attributed to the pyrite interface as a limiting factor for fabricating efficient pyrite-metal junctions [46].

$I$ – $V$  curve of pyrite-FeS<sub>2</sub>/NiO hetero-structure is seen in Fig. 5 (black). It is obvious that a junction between the pyrite and NiO deposited by SILAR (20 cycles) has been formed but no photocurrent is generated in this solar cell structure. The existence of the pinholes or defects on pyrite crystals' surfaces could be responsible for the leakage current in reverse bias. Future studies are needed to improve the working ability of the pyrite MGL solar cell structure.

Charge carrier concentrations found from  $C$ – $V$  measurements were  $6.2 \times 10^{16} \text{ cm}^{-3}$  for FeS<sub>2</sub>/NiO hetero-structures and  $2.5 \times 10^{17} \text{ cm}^{-3}$  for FeS<sub>2</sub>/Pt Schottky diodes. These results are in good accordance with the expected values based on literature data [47].

## 4. Conclusions

FeS<sub>2</sub> monograin powder was considered as an option for the absorber material in MGL solar cells for energy production in a future lunar habitat. In this work, the conditions for FeS<sub>2</sub> microcrystalline (monograin) powders by synthesis-growth method and a cooling procedure for retaining the pyrite phase of FeS<sub>2</sub> without formation of additional phases were found. Synthesis of FeS<sub>2</sub> from FeS and S was performed at 740 °C in molten KI for one week. Slow cooling to 575 °C and keeping the ampoule at this temperature for 24 h followed by rapid cooling to room temperature resulted in single phase pyrite monograin powder. Produced FeS<sub>2</sub> had cubic structure with lattice parameters  $a = b = c = 5.4154 \text{ \AA}$  characteristic to the pyrite phase of FeS<sub>2</sub>. Raman analysis (supported by XRD data) confirmed the pure pyrite phase. Powder crystals had round shape and  $n$ -type conductivity. Nearly half of the gained powder material was in the crystal size fraction of around 50  $\mu\text{m}$ . Schottky diodes with Pt as junction partner showed a rectifying junction. First solar cells based on pyrite monograin powder in monograin layer design were assembled with  $p$ -type NiO. The pyrite/NiO device showed a formation of rectifying junction between the materials, but no photocurrent was detected. These results may be improved by further work with surface treatments of the absorber crystals, different dopants, and pyrite junction partners.

## Declaration of competing interest

The authors declare that they have no known competing financial interests or personal relationships that could have appeared to influence the work reported in this paper.

## Acknowledgements

This work has been supported by the European Regional Development Fund, Project TK141, by the Estonian Research Council Grants PRG1023 and TT13 and European Space Agency Discovery programme under Contract no. 4000134676.

## References

- M. Braun, N.G. Veronica Trivino, S. Hosseini, R. Schonenborg, M. Landgraf, Human lunar return: an analysis of human lunar exploration scenarios within the upcoming decade, *Acta Astronaut.* (2020), <https://doi.org/10.1016/j.actaastro.2020.03.037>.
- J.N. Rasera, J.J. Cilliery, J.A. Lamamy, K. Hadler, The beneficiation of lunar regolith for space resource utilisation: a review, *Planet. Space Sci.* (2020), <https://doi.org/10.1016/j.pss.2020.104879>.
- M. Braun, N.G. Veronica Trivino, S. Hosseini, R. Schonenborg, M. Landgraf, Human lunar return: an analysis of human lunar exploration scenarios within the upcoming decade, *Acta Astronaut.* (2020), <https://doi.org/10.1016/j.actaastro.2020.03.037>.
- N.J. Bennett, D. Ellender, A.G. Dempster, Commercial viability of lunar in-situ resource utilization (ISRU), *Planet. Space Sci.* (2020), <https://doi.org/10.1016/j.pss.2020.104842>.
- M. Altaoara, et al., Monograin Layer Solar Cells, 2003, [https://doi.org/10.1016/S0040-6090\(03\)00167-6](https://doi.org/10.1016/S0040-6090(03)00167-6).
- E. Mellikov, et al., Monograin materials for solar cells, *Sol. Energy Mater. Sol. Cell.* (2009), <https://doi.org/10.1016/j.solmat.2008.04.018>.
- E. Mellikov, et al., Growth of CZTS-based monograin and their application to membrane solar cells, in: *Copper Zinc Tin Sulfide-Based Thin-Film Solar Cells, 2015*, <https://doi.org/10.1002/9781118437865.ch13>.
- C. Leiner, C. Sommer, V. Satzinger, L. Plessing, G. Peharz, CPV Membranes Made by Roll-To-Roll Printing: A Feasible Approach?, 2016, <https://doi.org/10.1063/1.4962100>.
- T. Raadik, Adapting Crystalsol Product to a Moon Environment, *ESA GSTP Small Studies*, 2016. [https://www.esa.int/Enabling\\_Support/Space\\_Engineering\\_Technology/Shaping\\_the\\_Future/Adapting\\_Crystalsol\\_product\\_to\\_a\\_moon\\_environment](https://www.esa.int/Enabling_Support/Space_Engineering_Technology/Shaping_the_Future/Adapting_Crystalsol_product_to_a_moon_environment).
- D.E. Wilhelms, Lunar stratigraphy and sedimentology, *Icarus* (1977), [https://doi.org/10.1016/0019-1035\(77\)90020-3](https://doi.org/10.1016/0019-1035(77)90020-3).
- G.A. Landis, Materials refining on the Moon, *Acta Astronaut.* (2007), <https://doi.org/10.1016/j.actaastro.2006.11.004>.
- J.M.D. Day, E.M.M.E. van Kooten, B.A. Hofmann, F. Moynier, Mare basalt meteorites, magnesian-suite rocks and KREEP reveal loss of zinc during and after lunar formation, *Earth Planet Sci. Lett.* (2020), <https://doi.org/10.1016/j.epsl.2019.115998>.
- M. Rahman, G. Boschloo, A. Hagfeldt, T. Edvinsson, On the mechanistic understanding of photovoltage loss in iron pyrite solar cells, *Adv. Mater.* (2020), <https://doi.org/10.1002/adma.201905653>.
- C. Steinhagen, T.B. Harvey, C.J. Stolle, J. Harris, B.A. Korgel, Pyrite nanocrystal solar cells: promising, or fool's gold? *J. Phys. Chem. Lett.* (2012) <https://doi.org/10.1021/jz301023c>.
- M. Limpinsel, M. Limpinsel, *Iron Pyrite Absorbers for Solar Photovoltaic Energy Conversion*, Irvine, 2015, 2015.
- M. Rahman, G. Boschloo, A. Hagfeldt, T. Edvinsson, On the mechanistic understanding of photovoltage loss in iron pyrite solar cells, *Adv. Mater.* (2020), <https://doi.org/10.1002/adma.201905653>.
- M.Z. Rahman, T. Edvinsson, What is limiting pyrite solar cell performance? *Joule* 3 (10) (Oct. 16, 2019) 2290–2293, <https://doi.org/10.1016/j.joule.2019.06.015>.
- M. Law, *Pyrite Iron Sulfide Solar Cells Made from Solution*, 2017. Irvine.
- M. Limpinsel, *Iron Pyrite Absorbers for Solar Photovoltaic Energy Conversion*, 2015. IRVINE.
- X. Zhang, et al., Potential resolution to the doping puzzle in iron pyrite: carrier type determination by Hall effect and thermopower, *Phy. Rev. Mat.* 1 (1, Jun. 2017), <https://doi.org/10.1103/PhysRevMaterials.1.015402>.
- M. Limpinsel, et al., An inversion layer at the surface of n-type iron pyrite, *Energy Environ. Sci.* 7 (6) (2014), <https://doi.org/10.1039/c3ee43169j>.
- M. Rahman, G. Boschloo, A. Hagfeldt, T. Edvinsson, On the mechanistic understanding of photovoltage loss in iron pyrite solar cells, *Adv. Mater.* 32 (26, Jul. 2020), <https://doi.org/10.1002/adma.201905653>.
- L.A. Taylor, K.L. Williams, *Cu-Fe-S Phases in Lunar Rocks*, 1973. Stanford, California.
- A.E. Saal, E.H. Hauri, Large Sulfur Isotope Fractionation in Lunar Volcanic Glasses Reveals the Magmatic Differentiation and Degassing of the Moon, Providence, USA, 2021 [Online]. Available: <https://www.science.org>.
- A.S. McEwen, M.S. Robinson, Mapping of the Moon by clementine, *Adv. Space Res.* 19 (10) (Jan. 1997) 1523–1533, [https://doi.org/10.1016/S0273-1177\(97\)00365-7](https://doi.org/10.1016/S0273-1177(97)00365-7).
- J. Ciążęła, M. Ciążęła, D. Marciniak, G. Paslawski, MIRORES) Multiplanetary Far-Infrared Spectrometer for Prospecting Deposit Minerals, *Institute of Geological Sciences, Polish Academy of Sciences*, 2017.
- R.V. Morris, Origins and size distribution of metallic iron particles in the lunar regolith, *Geochem. Cosmochim. Acta* 2 (1980) 1697–1712. Supplement.
- D. Vaniman, D. Pettit, G. Heiken, *Uses of Lunar Sulfur*, 1992.
- A. Colaprete, et al., Detection of water in the LCROSS ejecta plume, *Science* 330 (6003) (1979) 463–468, <https://doi.org/10.1126/science.1186986>. Oct. 2010.
- D. Vaniman, D. Pettit, G. Heiken, *Uses of lunar sulfur*, in: *2nd Conference on Lunar Bases and Space Activities*, 1992, pp. 429–435.
- M. Altaoara, et al., Monograin Layer Solar Cells, 2003, [https://doi.org/10.1016/S0040-6090\(03\)00167-6](https://doi.org/10.1016/S0040-6090(03)00167-6).
- D. Shishin, E. Jak, S.A. Decterov, Critical assessment and thermodynamic modeling of the Fe-O-S system, *J. Phase Equilibria Diffus.* (2015), <https://doi.org/10.1007/s11669-015-0376-4>.
- O.K. von Goldbeck, *IRON—Binary Phase Diagrams* (1982), <https://doi.org/10.1007/978-3-662-08024-5>.
- Y.-H. Chen, et al., Using the high-temperature phase transition of iron sulfide minerals as an indicator of fault slip temperature, *Sci. Rep.* 9 (1) (Dec. 2019) 7950, <https://doi.org/10.1038/s41598-019-44319-8>.
- Y. Akaltun, T. Çayır, Fabrication and characterization of NiO thin films prepared by SILAR method, *J. Alloys Compd.* 625 (Mar. 2015), <https://doi.org/10.1016/j.jallcom.2014.10.194>.
- P.P. Altermatt, T. Kiesewetter, K. Ellmer, H. Tributsch, Specifying targets of future research in photovoltaic devices containing pyrite (FeS<sub>2</sub>) by numerical modelling, *Sol. Energy Mater. Sol. Cell.* 71 (2) (Feb. 2002) 181–195, [https://doi.org/10.1016/S0927-0248\(01\)00053-8](https://doi.org/10.1016/S0927-0248(01)00053-8).
- H. Xian, et al., Hydration induced bandgap shift at pyrite-water interface, *Appl. Phys. Lett.* 113 (12) (Sep. 2018) 123901, <https://doi.org/10.1063/1.5048542>.
- K.P. Bhandari, et al., Iron pyrite nanocrystal film serves as a copper-free back contact for polycrystalline CdTe thin film solar cells, *Sol. Energy Mater. Sol. Cell.* 140 (Sep. 2015) 108–114, <https://doi.org/10.1016/j.solmat.2015.03.032>.
- L. Wu, et al., Enhanced photoresponse of FeS<sub>2</sub> films: the role of marcasite-pyrite phase junctions, *Adv. Mater.* 28 (43, Nov. 2016), <https://doi.org/10.1002/adma.201602222>.
- F. Gossenberger, T. Roman, K. Forster-Tonigold, A. Groß, Change of the work function of platinum electrodes induced by halide adsorption, *Beilstein J. Nanotechnol.* 5 (Feb. 2014) 152–161, <https://doi.org/10.3762/bjnano.5.15>.
- H. Vogt, T. Chattopadhyay, H.J. Stolz, Complete first-order Raman spectra of the pyrite structure compounds FeS<sub>2</sub>, MnS<sub>2</sub> AND SiP<sub>2</sub>, *J. Phys. Chem. Solid.* (1983), [https://doi.org/10.1016/0022-3697\(83\)90124-5](https://doi.org/10.1016/0022-3697(83)90124-5).
- A.N. Utyuzh, Influence of temperature on Raman spectra of the FeS<sub>2</sub> single crystal with pyrite structure, *Phys. Solid State* (2014), <https://doi.org/10.1134/S1063783414100321>.
- A. Zavrazhnov, A. Naumov, A. Kosyakov, S. Berezin, V. Volkov, A. Sergeeva, The iron sulfides crystal growth from the halide melts, *Mater. Res.* (2018), <https://doi.org/10.1590/1980-5373-mr-2017-0648>.
- P. Prabukanthan, S. Thamaraiselvi, G. Harichandran, Single step electrochemical deposition of p-type undoped and Co<sup>2+</sup> doped FeS<sub>2</sub> thin films and performance in heterojunction solid solar cells, *J. Electrochem. Soc.* (2017), <https://doi.org/10.1149/2.0991709jes>.
- H. Ning, Z. Liu, Y. Xie, H. Huang, CoS<sub>2</sub> coatings for improving thermal stability and electrochemical performance of FeS<sub>2</sub> cathodes for thermal batteries, *J. Electrochem. Soc.* (2018), <https://doi.org/10.1149/2.0321809jes>.
- K.K. Mishra, K. Osseo-Asare, Fermi Level Pinning at Pyrite (FeS<sub>2</sub>)/Electrolyte Junctions, 1992.
- Z. Shi, A.H. Jayatissa, Preparation and characterization of cobalt-doped iron pyrite (FeS<sub>2</sub>) thin films, *Prog. Nat. Sci.: Mater. Int.* 30 (3, Jun. 2020), <https://doi.org/10.1016/j.pnsc.2020.03.002>.